
This is an electronic reprint of the original article.
This reprint may differ from the original in pagination and typographic detail.

Wechsuwanmanee, Peerapon; Lian, Junhe; Münstermann, Sebastian

3D Multilevel Modeling of Surface Roughness Influences on Hole Expansion Ratios

Published in:
Steel Research International

DOI:
[10.1002/srin.202100449](https://doi.org/10.1002/srin.202100449)

Published: 01/12/2021

Document Version
Publisher's PDF, also known as Version of record

Published under the following license:
CC BY

Please cite the original version:
Wechsuwanmanee, P., Lian, J., & Münstermann, S. (2021). 3D Multilevel Modeling of Surface Roughness Influences on Hole Expansion Ratios. *Steel Research International*, 92(12), Article 2100449. <https://doi.org/10.1002/srin.202100449>

3D Multilevel Modeling of Surface Roughness Influences on Hole Expansion Ratios

Peerapon Wechsuwanmanee,* Junhe Lian, and Sebastian Münstermann

The steel grade DP1000 is widely used in various industrial application fields. Its mechanical properties satisfy basic requirements in terms of strength and global formability due to the tailored microstructure composed of ductile ferrite and hard martensite. Nevertheless, the edge crack sensitivity of dual-phase steels is still of interest. For its evaluation, hole expansion tests have become a standard experimental approach. Finite element simulation is a tool that further supports the assessment of edge crack resistance by providing insights into local stress and strain fields at the formed edges during hole expansion tests. However, there are still discrepancies between the experiments and simulations in terms of force–displacement curves and hole expansion ratios due to several factors including the hole edge surface condition. To overcome these discrepancies, this work proposes a 3D multiscale simulation strategy to quantify this factor under a complex loading case and to include it into the simulation approaches. The workflow is sufficiently general to handle arbitrary load cases. Compared with state-of-the-art ductile damage mechanics simulations, the accuracy of the simulations is significantly improved.

category. They demonstrate their mechanical behaviors in an exceptional way. Their microstructure, which is composed of a ferritic matrix and martensitic islands, helps to fulfill the property requirements in particular with respect to strength, strain hardening, ductility, and crashworthiness. However, early fracture during mechanical loading is still observed,^[2,3] in particular when the local state of stress is challenging. As the AHSS encounters complex failure behaviors, the primary failure mechanism for them is ductile damage which is a result of void nucleation, void growth, and void coalescence.^[1–5]

Hole expansion test (HET) is one of the most important tests to evaluate cold formability for AHSS. As this test is a destructive evaluation, each test costs time and resources. Therefore, attempts are made to replace these experiments by meaningful numerical simulations, in which typically damage mechanics models are applied to

allow for predicting damage and fracture. Recently, the modified Bai–Wierzbicki (MBW) model^[3,4,6] has been presented and proven able to provide accurate damage and fracture predictions even for complex strain paths. The MBW model is a macroscopic phenomenological ductile damage mechanics model. It uses strain-based and stress-state dependent criteria for damage initiation and ductile fracture. Because this model evaluates the equivalent plastic strain to decide whether ductile damage mechanisms have been activated, it is generally prone to consider strain localization effects resulting from surface roughness profiles. The main obstacle that has to be overcome is the different scales because the element edge length for the macroscopic simulations is much bigger than the surface roughness characteristics. Obviously, a scalebridging approach is required, in which strain localization due to surface roughness is evaluated on the lower scale, while macroscopic predictions are based on the evaluations on the coarser scale. The problem is therefore partly shifted to the question of interaction between the simulations on those two different scales, and a solution approach will be presented in this article.


In general, damage mechanics models can be categorized into uncoupled and coupled ones.^[7] A renowned example of the uncoupled class is the Johnson–Cook model.^[8] It considers fracture strain as a function of triaxiality η . Later, it has been discovered that not only the triaxiality η affects the fracture strain, but also Lode angle parameter $\bar{\theta}$, which are calculated from invariants of stress tensors and the deviatoric stress tensor,

1. Introduction

Advanced high strength steel (AHSS) has been playing a crucial role in many industries. One of the industries that paid its time and effort the most toward developing steels with outstanding properties is the automotive industry. It has been focusing its properties not only in terms of global strength but also in terms of local strength to accomplish the formability condition.^[1] Dual-phase steels are prominent and widely used members of this

P. Wechsuwanmanee, S. Münstermann
Steel Institute
RWTH Aachen University
Intzestraße 1, 52072 Aachen, Germany
E-mail: peerapon.wechsuwanmanee@rwth-aachen.de

J. Lian
Advanced Manufacturing and Materials, Department of Mechanical Engineering
Aalto University
Otakaari 4, 02150 Espoo, Finland

 The ORCID identification number(s) for the author(s) of this article can be found under <https://doi.org/10.1002/srin.202100449>.

© 2021 The Authors. Steel Research International published by Wiley-VCH GmbH. This is an open access article under the terms of the Creative Commons Attribution-NonCommercial License, which permits use, distribution and reproduction in any medium, provided the original work is properly cited and is not used for commercial purposes.

DOI: 10.1002/srin.202100449

respectively.^[9] A combination of η and $\bar{\theta}$ is called stress-state. It indicates how the local material experiences the loading.

Surface condition has been considered as a factor in the material integrity already for decades. Most of research attention has been paid to cyclic loading and fatigue.^[10–13] The main factor from surface condition which contributes to material degradation and failure is its roughness component. In other words, the roughness is considered as the geometrical imperfection that causes localization during the operation.^[14] Some evidence indicates that different roughness levels on samples, in particular, ground samples and polished samples, result in different response on cyclic loading^[13] as well as in-plane strain loading.^[15] Finite element (FE) model with roughness consideration in cyclic loading can be found in Ås et al.^[12] In addition, McMillan et al.^[16] propose a technique to model roughness geometry based on Minkowski curve^[17] in axisymmetric loading. A multiscale strategy has been introduced at first in cold forming application in plane strain loading case.^[18] However, there are still limitations using this approach as this technique relies on an assumption that the surface height distribution must obey a specific random distribution function to apply that function to generate the representative surface in the micromodel. The surface height at different points on the spatial domain with fixed interval is randomly picked based on that distribution function. Later, an extension to the MBW model regarding surface condition has been introduced.^[15] It adds an additional surface factor as a multiplier to lower the damage initiation criteria as well as fracture criteria of the elements at the surface to reflect the vulnerability of the surface comparing to the bulk material. Still, a limitation for this approach is the representative surface generation in 2D. Therefore, it is well applicable to loading cases that can be simplified to 2D problems, but not general complex loading applications. In addition, the approach indicates that the point interval on the representative surface is chosen based on a fixed number from the wavelength of which noise is expected. With this approach, there is a chance of high height gradient during the artificial surface generation which causes the submodel being too fragile than it should be. This work therefore provides a general solution that suits arbitrary loading cases in 3D with a novel artificial surface generation approach that is independent from point interval manual selection.

2. MBW Material Model with Surface Roughness Correction

Given σ_1 , σ_2 , and σ_3 as the three principal stresses, the three invariants p , q , and r of the stress tensor read

$$p = -\sigma_m = -\frac{1}{3}(\sigma_1 + \sigma_2 + \sigma_3) \quad (1)$$

$$q = \bar{\sigma} = \sqrt{\frac{1}{2} \cdot [(\sigma_1 - \sigma_2)^2 + (\sigma_2 - \sigma_3)^2 + (\sigma_3 - \sigma_1)^2]} \quad (2)$$

$$r = \left[\frac{27}{2} \cdot (\sigma_1 - \sigma_m)(\sigma_2 - \sigma_m)(\sigma_3 - \sigma_m) \right]^{\frac{1}{3}} \quad (3)$$

The triaxiality η and Lode angle θ are defined by

$$\eta = -\frac{p}{q} \quad (4)$$

$$\theta = \frac{1}{3} \cdot \arccos \left[\left(\frac{r}{q} \right)^3 \right] \quad (5)$$

The Lode angle ranges between $0 \leq \theta \leq \pi/3$. By normalizing it, the normalized Lode angle or Lode angle parameter $\bar{\theta}$ which has its range of $-1 \leq \bar{\theta} \leq 1$ is achieved by

$$\bar{\theta} = 1 - \frac{6\theta}{\pi} \quad (6)$$

On the contrary, the coupled model category indicates the degradation of the material by a damage-induced softening variable D . This variable can be a scalar or a tensor depending on the model,^[19] which can be applied onto the yield potential as well as damage evolution law after the onset of the damage.^[3] This work considers the MBW model which demonstrates a hybrid behavior between uncoupled and coupled model according to Wu et al.^[4] The yield potential Φ describing isotropic hardening is defined by

$$\Phi = \bar{\sigma} - (1 - D) \cdot \sigma_{yld} \leq 0 \quad (7)$$

where $\bar{\sigma}$ is the von Mises equivalent stress, σ_{yld} is the material flow stress, and D is a scalar damage variable. The plastic deformation after yielding at the first stage considers only strain hardening effects. In other words, the damage variable is turned off as long as $D = 0$. It starts to play a role upon the time instant that the equivalent plastic strain $\bar{\epsilon}^p$ reaches the stress-state dependent ductile damage initiation locus (DIL) $\bar{\epsilon}^i$, which reads

$$\bar{\epsilon}^i(\eta, \bar{\theta}) = c_s [(c_1^i \cdot \exp(-c_2^i \cdot \eta) - c_3^i \cdot \exp(-c_4^i \cdot \eta)) \bar{\theta}^2 + c_3^i \cdot \exp(-c_4^i \cdot \eta)] \quad (8)$$

$$c_s = \frac{\bar{\epsilon}_{meso}^i}{\bar{\epsilon}_{micro}^i} \quad (9)$$

where c_1^i , c_2^i , c_3^i , and c_4^i are DIL parameters to be calibrated from mechanical experiments. The surface factor c_s was introduced in Wechsuanmanee et al.^[15] to incorporate the fact that surface imperfection plays a role in local material softening during deformation. This factor is ranged between $0 \leq c_s \leq 1$ for the material point on the surface and $c_s = 1$ on the bulk material. It is calculated by the ratio between the damage initiation plastic strain of the meso-level $\bar{\epsilon}_{meso}^i$ and the damage initiation plastic strain in the micro-level $\bar{\epsilon}_{micro}^i$ in the multiscale analysis. The surface factor calibration process is discussed in the upcoming paragraph. As the damage is initiated on the material point, the material degradation affects not only the damage-induced softening as the deformation progresses, but also the elastic modulus during unloading. Given the initial elastic modulus denoted by E_0 , the effective elastic modulus E_{eff} reads

$$E_{eff} = (1 - D) \cdot E_0 \quad (10)$$

Once the damage initiation criterion is fulfilled, the damage evolution law applies to indicate how the damage variable D evolves. It is assumed to be a linear relationship between the

damage D and the equivalent plastic strain $\bar{\epsilon}^p$ with dissipation energy G_f as its characteristic slope in the special case of proportional loading. The damage D is formulated by

$$D = \begin{cases} 0, & \bar{\epsilon}^p \leq \bar{\epsilon}^i \\ \frac{\sigma_{\text{yld},i}}{G_f} \int_{\bar{\epsilon}^i}^{\bar{\epsilon}^p} d\bar{\epsilon}^p, & \bar{\epsilon}^i < \bar{\epsilon}^p < \bar{\epsilon}^f \\ 1, & \bar{\epsilon}^f \leq \bar{\epsilon}^p \end{cases} \quad (11)$$

The damage is set to be unity $D = 1$ once the equivalent plastic strain $\bar{\epsilon}^p$ exceeds the ductile fracture locus (DFL) which is defined by fracture strain $\bar{\epsilon}^f$

$$\bar{\epsilon}^f(\eta, \bar{\theta}) = c_s \left[(c_1^f \cdot \exp(-c_2^f \cdot \eta) - c_3^f \cdot \exp(-c_4^f \cdot \eta)) \bar{\theta}^2 + c_3^f \cdot \exp(-c_4^f \cdot \eta) \right] \quad (12)$$

where c_1^f , c_2^f , c_3^f , and c_4^f are DFL parameters to be calibrated. This DFL plays a role as a fracture criterion for the material element deletion step of the numerical simulation. The current development of MBW supports nonproportional loading by considering damage initiation indicators, which are based on DIL evaluations.^[20] This allows us to investigate the local complex loading case in the HET.

3. Materials and Testing

This study selected DP1000, a dual-phase steel grade with ultimate tensile strength of approximately 1000 MPa, with thickness of 1.5 mm. This steel grade is one of the most widely used steel grades in the automotive industry. The microstructure is composed of 62% ferrite and 38% martensite. The benefits of using this steel grade compared with other dual-phase steel grades are the strength from the martensite structure as well as the fine grain structure of the ferrite which leads to exceptional overall strength without trading off the risk of embrittlement. Detailed investigations of this steel are found in Münstermann et al.^[21] A brief summary of their discoveries is discussed here. The chemical composition of DP1000 is shown in **Table 1**.

Uniaxial tensile tests on flat samples at quasistatic strain rate and at room temperature were performed on this steel to achieve its standard mechanical properties to describe its elastic and plastic behaviors which are shown in **Table 2**. The achieved flow curve can be extrapolated by

$$\sigma_{\text{yld}} = k \cdot (\bar{\epsilon}^p)^{n_H} \quad (13)$$

where σ_{yld} is yield stress, $\bar{\epsilon}^p$ is equivalent plastic strain, k and n_H are parameters to be calibrated from the uniaxial tensile experiments.

Equation (13) assumes that the material can deform infinitely without considering material degradation and fracture. The MBW

Table 2. Mechanical properties of DP1000.

	E [GPa]	ν [-]	$R_{p0.2}$ [MPa]	R_m [MPa]	A_g [%]	A_{80} [%]	k [MPa]	n_H [-]
DP1000	210	0.3	693	1039	8.1	12.0	1476	0.10

material model is utilized to add damage and fracture properties into the evaluation. A hybrid strategy to find the best agreement between experiments and numerical simulations was deployed. This curve fitting strategy relies on different sample geometries representing different stress states that are expressed in terms of stress triaxiality and Lode angle parameter. The entire procedure aims to find one set of parameters that allows to reproduce all the experimental results which are typically expressed in terms of force–displacement curves. Noteworthy, particular interest is laid on the prediction of fracture events because this feature is the most important one when it later comes to the simulation of HETs. The mechanical tests evaluated to identify the MBW model parameters comprise notched dog-bone samples, central hole samples, notched plane strain samples, and shear samples. All tests were performed at quasistatic, and at room temperature setting, with three repeats each. The corresponding tensile test samples were simulated in ABAQUS with flow curve given in Eq. (13). The force–displacement curves from experiments and simulations were compared to ensure the representability of the plastic behavior. Upon damage initiation and fracture in the experiments, the equivalent plastic strain, stress triaxiality, and Lode angle parameters from different geometries were recorded to fit the curves in Equation (8) and (12). **Table 3** shows the result of the parameter calibration for the selected steel of grade DP1000.

3.1. HET

HET is one of the most widely used approaches to characterize the edge crack resistance of sheet metals for applications in the automotive industry. **Figure 1** shows the experimental setup of the test. This test is composed of four components—sheet sample, conical punch, die, and blank holder as shown in **Figure 1a**. Initially, the hole diameter is D_0 . After testing as shown in **Figure 1b**, the free edge of the hole will be bent and single or multiple cracks will appear. Thereby the hole is widened so that the diameter D_h can be measured. The ratio between the initial hole diameter and the hole diameter after testing is generally the indicator to evaluate edge crack sensitivity of the sheet sample.

The 1.5 mm-thick sheet was manufactured into 110 mm width octagon with 10 mm diameter hole at its center. The geometry is designed to be clamped by a die with 90 mm diameter. The overall dimension of the sheet is shown in **Figure 2a**. According to ISO16630,^[22] the hole shall be manufactured by punching process. However, this article aims to study only geometrical effects on surface roughness of the edge, while the punching process induces a huge amount of residual stress on the edge surface

Table 1. Chemical composition of DP1000, mass content in %.

	C	Si	Mn	P	Cr	Mo	Ni	Cu	N
DP1000	0.140	0.320	1.970	0.011	0.400	0.050	0.0370	0.023	<0.0001

Table 3. MBW model parameter set for DP1000.^[35]

Parameter	c_1^f	c_2^f	c_3^f	c_4^f	G_f	c_1^f	c_2^f	c_3^f	c_4^f
Value	0.40	1.00	0.10	1.50	6500	0.15	1.50	0.08	1.50

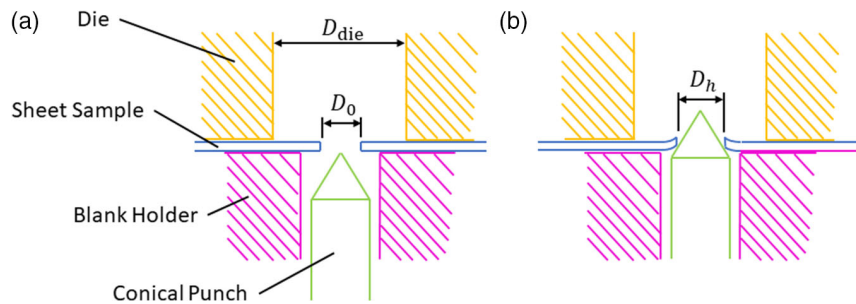


Figure 1. Schematic of HET a) before testing and b) after testing.

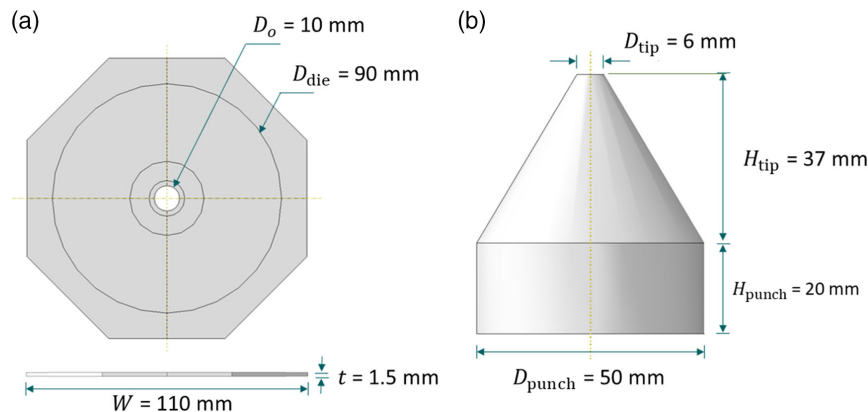


Figure 2. a) Hole expansion sheet dimension and b) conical punch dimension.

in addition. To minimize the unwanted effect from the residual stress, wire cutting was selected to manufacture the hole. Therefore, it has to be noted that well-known predamage effects from machining are less dominant compared with the geometrical imperfection effect in this special case.

The samples were loaded by a conical punch with geometry, as shown in Figure 2b. The conical angle of this punch is $\approx 60^\circ$. The punch is equipped in a universal testing machine Erichsen 142/40. The punch moves upward at the speed of 5 mm min^{-1} at room temperature such that the isothermal condition and the quasistatic condition are satisfied. Thus, no strain-rate effect as well as no thermal effect is involved during the deformation. The loading applies until a through-thickness crack appears. During the loading, reaction force and displacement of the punch are recorded. At the end of the test, hole expansion ratio (HER) is calculated by

$$\text{HER} = \frac{D_h - D_o}{D_o} \times 100 \quad (14)$$

where D_o and D_h are average original hole diameter and average hole diameter after fracture respectively. To ensure the repeatability, ten samples were taken into the test.

3.2. Surface Topography Measurement

To obtain a quantitative description of edge surface topography from different manufacturing techniques, the HET sample surfaces were analyzed by a confocal microscope of the type

NanoFocus $\mu\text{soft explorer}$. The machine applies the confocal multipinhole (CMP) technology. It allows to measure the topography of a specimen by sending light through pinhole's disc and lens at different focusing distances. This action generates light reflection on the camera sensor and is sequentially transformed into surface information.

Undeformed HET samples were cut into a quarter. To ensure the repeatability, four cut pieces were taken into the topology measurement. During the measurement, the edge surface was mounted upright to be normal to the light source. The measurement takes 20:1 amplification lens, lens aperture (f -value) 0.45, shutter speed 1/100 s, ISO 100. This setting achieves $1.6 \mu\text{m}$ in-plane resolution (x -, y -direction) and 5 nm out-of-plane resolution (z -direction). Each measurement covers $1.475 \text{ mm} \times 1.475 \text{ mm}$ area. Due to the hole edge curvature, the actual area coverage becomes $0.7 \text{ mm} \times 1.475 \text{ mm}$, as show in **Figure 3**.

4. Surface Roughness Characterization

The surface topography from confocal microscope cannot be analyzed in its raw format. Instead, the data have to be processed before it can be used in the numerical framework for roughness effect evaluation. A first processing step is needed to distinguish between waviness and roughness components^[23] because only roughness leads to the localization of strain that affects the edge crack sensitivity. To give definitions, waviness is a profile holding long wavelength components, so they are appearing on a relatively broad scale. In contrast, roughness is a profile holding short wavelength components, therefore expressing itself in

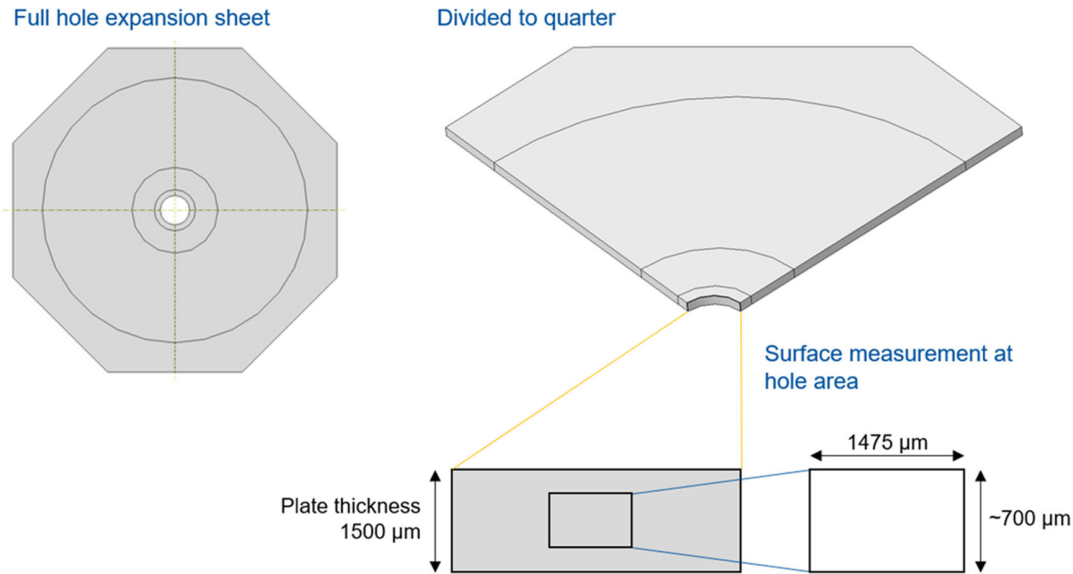


Figure 3. Topography measurement region.

surface height variations in miniature scale. The waviness component can be imagined as a smoothened version of the raw surface. Consequently, the roughness is nothing but the residual from the subtraction between raw surface and waviness. In manufacturing technology, roughness is usually the initial surface condition of the material, while waviness results from cutting tools marks or equipment imbalance.^[24]

4.1. Discrete Fourier Transformation

To achieve the waviness and roughness information, the surface measurement signal shall be considered as spatial signal. To be more concise, a definition of signal by a physical quantity which is varied by time or other independent parameter which is equally spaced is demonstrated.^[25] In this case, the independent parameters are distance from the origin in x - and y -direction. A general framework to apply Gaussian filter directly onto the spatial signal in 1D is introduced in.^[26] It is possible to analyze the surface profile in 1D independently for each direction, and combines the results afterward. However, this approach consequently distorts the correlation between the two directions. Later, areal Gaussian filter to process the 2D spatial signal became a standard workflow.^[27] Nevertheless, these approaches limit interpretability of the signal and variety of signal processing tools as they are still in the spatial domain. On the contrary, transforming signals from the spatial domain into the frequency domain using Fourier transformation (FT) enhances the analysis for three reasons^[28]: 1) most of real-world signals are superimposed sinusoids, 2) sinusoids have linear characteristics, so that their frequencies remain after modification, and 3) there are broad numbers of mathematical tools and programming algorithms available for the analysis.

FT is a mathematical technique aiming to decompose signals into a set of sinusoids at different frequencies.^[28] The word frequency ω in this context is nothing but an inverse of the

wavelength λ ($\omega = 1/\lambda$). As a result, a signal component with short wavelength is implied as high frequency and a signal component with long wavelength yields low frequency. In addition, one can transform the processed signal in frequency domain back to time domain or spatial domain by applying inverse Fourier transformation (IFT). The operation directions of FT and IFT are shown in **Figure 4**.

As the white-light confocal microscope provides the topography spatial data in discrete format, it contains N and M sampling points of surface height in x - and y -direction, respectively, thus $N \times M$ sampling points in total. The distance between each data point is given by the lens in-plane resolution. The discrete Fourier transformation and inverse Fourier transformation between spatial domain $f(x, y)$ and the frequency domain $F(u, v)$ are defined by^[29]

$$F(u, v) = \sum_{x=0}^{N-1} \sum_{y=0}^{M-1} f(x, y) \exp \left[-2\pi j \left(\frac{ux}{N} + \frac{vy}{M} \right) \right] \quad (15)$$

$$f(x, y) = \frac{1}{NM} \sum_{u=0}^{N-1} \sum_{v=0}^{M-1} F(u, v) \exp \left[2\pi j \left(\frac{ux}{N} + \frac{vy}{M} \right) \right] \quad (16)$$

Or in wavelength form

$$F(\lambda_x, \lambda_y) = \sum_{x=0}^{N-1} \sum_{y=0}^{M-1} f(x, y) \exp \left[-2\pi j \left(\frac{x}{N\lambda_x} + \frac{y}{M\lambda_y} \right) \right] \quad (17)$$

$$f(x, y) = \frac{1}{NM} \sum_{\lambda_x=0}^{N-1} \sum_{\lambda_y=0}^{M-1} F(\lambda_x, \lambda_y) \exp \left[2\pi j \left(\frac{x}{N\lambda_x} + \frac{y}{M\lambda_y} \right) \right] \quad (18)$$

in which

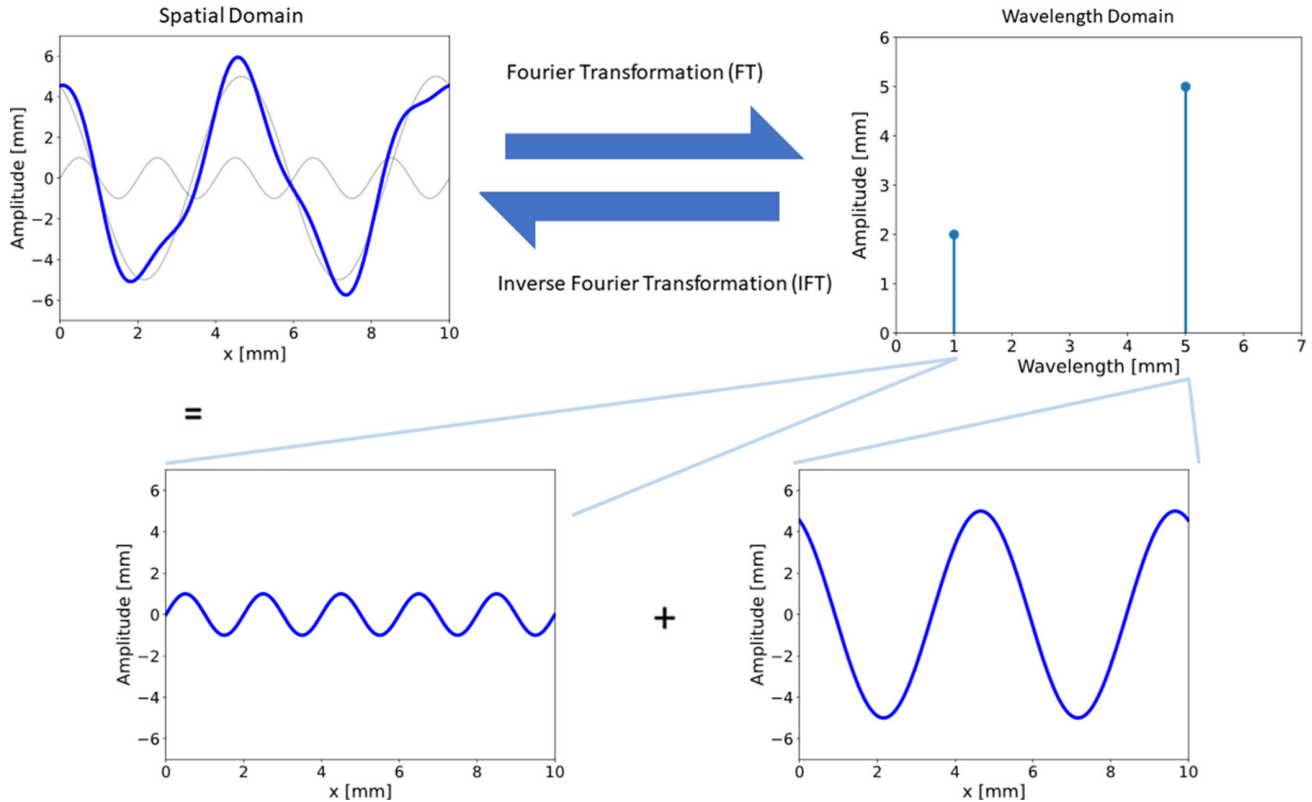


Figure 4. Operation directions of forward Fourier transform and inverse Fourier transform.

$$\exp \left[2\pi j \left(\frac{x}{N\lambda_x} + \frac{y}{M\lambda_y} \right) \right] = \cos \left[2\pi \left(\frac{x}{N\lambda_x} + \frac{y}{M\lambda_y} \right) \right] + j \sin \left[2\pi \left(\frac{x}{N\lambda_x} + \frac{y}{M\lambda_y} \right) \right] \quad (19)$$

where x, y are the location in spatial domain in x - and y -direction; u, v are the frequency components in frequency domain in x - and y -direction; λ_x, λ_y are the wavelength components in frequency domain in x - and y -direction; $\exp()$ is an exponential function; j is the imaginary unit satisfying the equation $j^2 = -1$. Each of the frequency components contains its weight in complex number—the so-called Fourier coefficient. It specifies how much a particular sinusoid with this frequency contributes to the signal in the spatial domain. While the signal in spatial domain demonstrates visible surface topography, the transformed signal in frequency domain represents linear combinations of infinite complex weights, Fourier coefficients $F(\lambda_x, \lambda_y)$, with 2D sinusoidal functions, cosine and sine, yielding from complex exponentials, $\exp \left[2\pi j \left(\frac{x}{N\lambda_x} + \frac{y}{M\lambda_y} \right) \right]$. Multiplying complex weight with sinusoidal function leads to a sinusoid with corresponding amplitude and phase. The Fourier transformation^[30] is implemented in `scipy.fft` module.^[31]

4.2. Convolution and Filters

Convolution is a mathematical operation that combines two signals to produce a resulting signal. This output signal indicates how

the primary signal is modified by the secondary one.^[28] The secondary signal is called filter kernel. The main task of the filter in this application is to extract waviness and roughness out of the raw surface. The convolution operation can be done in both spatial domain and frequency domain. The convolution operation in spatial domain can be found in Wechsuanmanee et al.^[18] The resulting roughness was aggregated as a normal distribution function. The surface condition in the multiscale simulation was generated by a random function based on this normal distribution curve. This approach works well under two conditions: 1) the surface shape is isotropic; 2) the resulting roughness after filtering satisfies normal distribution curve. Furthermore, it relies on a stochastic process during submodel generation. To ensure generalization, additional statistical analysis is required. In contrast, processing surface signal in frequency domain including convolution allows us to reconstruct the surface back to spatial domain using inverse Fourier transformation. The submodel generation process becomes deterministic because there is no longer random function involved.

There are two types of filters to be introduced for this application. The first one is low-pass filter $L(\lambda_x, \lambda_y)$ and another one is high-pass filter $H(\lambda_x, \lambda_y)$ which are defined by^[32]

$$L(\lambda_x, \lambda_y) = \exp \left\{ -\pi\beta \left[\left(\frac{\lambda_{xc}}{\lambda_x} \right)^2 + \left(\frac{\lambda_{yc}}{\lambda_y} \right)^2 \right] \right\} \quad (20)$$

$$H(\lambda_x, \lambda_y) = 1 - L(\lambda_x, \lambda_y) \quad (21)$$

where $\beta = \ln 2 / \pi = 0.2206$ and $\lambda_{xc}, \lambda_{yc}$ are the cutoff wavelengths in x - and y -direction. The low-pass filter allows the signal with

low frequency or long wavelength to pass through without modification while blocking the high frequency or short wavelength components. The cutoff wavelengths $\lambda_{xc}, \lambda_{yc}$ identify from which wavelength should the signal pass through or be blocked. The attenuation ratio of the filter becomes 50% when $\lambda_x = \lambda_{xc}$ with $\lambda_y = \infty$ or $\lambda_y = \lambda_{yc}$ with $\lambda_x = \infty$. Given raw surface measurement in frequency domain $Z(\lambda_x, \lambda_y)$, waviness $W(\lambda_x, \lambda_y)$ reads

$$W(\lambda_x, \lambda_y) = Z(\lambda_x, \lambda_y) * L(\lambda_x, \lambda_y) \quad (22)$$

where $*$ is convolution operator. As this convolution operation is performed in frequency domain, the calculation is basically an element-wise multiplication. Analogously, the roughness component in frequency domain $R(\lambda_x, \lambda_y)$ reads

$$R(\lambda_x, \lambda_y) = Z(\lambda_x, \lambda_y) * H(\lambda_x, \lambda_y) = Z(\lambda_x, \lambda_y) - W(\lambda_x, \lambda_y) \quad (23)$$

The high-pass and low-pass Gaussian filters in the frequency domain are shown in Figure 5a,b, respectively.

In general, the raw surface components can be distinguished into four groups ranging from the highest to the lowest wavelength—measurement inclination, waviness, roughness, and noise. They are decomposed by applying the low-pass filter from Equation (20) and high-pass filter from Equation (21) with different cutoff wavelengths $\lambda_{xc}, \lambda_{yc}$. This work assumes the isotropic surface condition of the hole edge. Therefore, $\lambda_{xc} = \lambda_{yc} = \lambda_c$ at every condition. The high-pass filter with flat wavelength $\lambda_f = 450 \mu\text{m}$ is selected as the first cutoff to decompose the measurement inclination from other components to adjust them to the horizontal level. This number is selected according to the confocal microscope measurement region after trimming the unusable outer area. Next, the low-pass filter with short wavelength $\lambda_s = 1 \mu\text{m}$ is used to remove noise from the signal by assuming that surface components with lower wavelength should not impact significantly in the damage initiation and evolution during the HET. The remaining components are then waviness and roughness. They are decomposed using a filter with $\lambda_c = 30 \mu\text{m}$ which is the size of the submodel in the multiscale FE simulation.

4.3. Dominant Wavelength Selection

The Fourier transformation describes an arbitrary signal in terms of linear combination of infinite number of sinusoids with different amplitudes and phases in theory. In fact, the implementation of Fourier transformation gives a finite number of sinusoids, but the overall number is still huge. To take every wavelength into account during surface reconstruction, the calculation may take too long for one analysis. In addition, most of the wavelengths contribute only tiny amplitudes which require high resolution in FE model, i.e., small mesh size, to cope with. In fact, these wavelengths are negligible. Therefore, selecting only dominant wavelengths to generate a simplified artificial surface speeds up the calculation drastically while minimizing surface distortion. To evaluate the distortion, a so-called R -squared metric (R^2) is taken into account. It is defined by^[33]

$$R^2(z, \hat{z}) = 1 - \frac{\sum_{i=0}^{N-1} (z_i - \hat{z}_i)^2}{\sum_{i=0}^{N-1} (z_i - \bar{z})^2} \quad (24)$$

where z is the surface height taking every wavelength into account, \bar{z} is the average of the surface height z , and \hat{z} is the simplified artificial surface height. Both z and \hat{z} contains N data points. This metric indicates the correlation between variance of artificial surface height and total variance of the reference data which is the average of z . This number ranges between -1.0 and 1.0 where 1.0 means the artificial data and reference data are perfectly correlated while the negative value implies inversed correlation. The $R^2 = 0.0$ specifies that the artificial data \hat{z} yields a constant value; in other words, a flat surface. The dominant wavelengths from 10% to 100% with 10% interval are considered. The minimum number of wavelengths with R^2 higher than 0.9 is selected.

The selected wavelength components can be reconstructed into an artificial surface by applying Equation (18) accordingly. Raster points with predefined resolution in x - and y -direction are sampled across the given surface area yielding its corresponding height z to export to FEM software afterward.

5. FE Model

This work applies multiscale FE simulation strategy to fulfill the fact that the HET sample is of mm-length while the surface

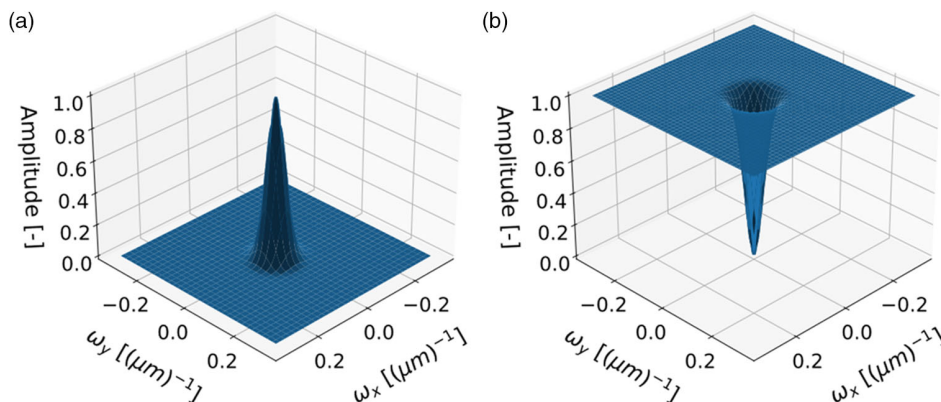


Figure 5. The amplitude transmission characteristic: a) low-pass Gaussian filter; b) high-pass Gaussian filter.

imperfection is of μm -length. Submodeling technique plays a crucial role in this strategy. The HET simulation with J2-plasticity material model is performed to obtain the global responses as well as local responses at the critical region. The local information is transferred to the submodel as its boundary conditions at the location where damage initiation criteria are satisfied. The original surface of the submodel at the free edge of the hole is then replaced by artificial surface geometry considering surface roughness profiles. The surface factor c_s is obtained at this stage according to Equation (9). Therefore, the fully calibrated MBW material model with surface factor is then applied to the free edge region of the HET simulation. As a result, it yields closer force–displacement response to the experimental results than the response from the conventional MBW model without the surface factor.

5.1. Macroscopic Model

The hole expansion sheet FE geometry as well as the punch are constructed in ABAQUS according to Figure 2a,b, respectively. The sheet geometry is reduced to be 1/36th model; in other words, 10° revolution to speed up the simulation process. The reduced sheet is divided into five regions from A to E as indicated in Figure 6. The meshing scheme is exploited into three levels—fine mesh of size $30\mu\text{m}$ on region A, medium mesh of size $100\mu\text{m}$ on region B, and coarse mesh of size $200\mu\text{m}$ on the remaining regions. Hexahedral brick elements with reduced integration (C3D8R) are allocated to every element on the sheet. The punch, however, is defined as an analytical rigid body; thus, no meshing is involved.

Fixed boundary conditions are defined on the top and bottom surfaces in region E of the sheet. On one side of the sheet, symmetry boundary conditions can easily be applied. Nevertheless, on the other side, a local coordinate system is applied to define its symmetry boundary condition. As this boundary condition is applied onto the local coordinate, a boundary condition redundancy will appear at the edge between the top/bottom surfaces of region E, where the fixed boundary conditions on the global coordinate are defined, and these side surfaces, where the symmetry boundary condition on the with local coordinate is used. To avoid this issue, a small gap of size equal to the coarse mesh size, $200\mu\text{m}$ in this case, is made at the region D. This setup trade-offs a slight discrepancy comparing with the 360° fully revolved geometry with a huge computational efficiency. The punch, as a rigid body, is defined to move upward; in other

words, in $+y$ -direction for 18 mm quasistatically. The friction coefficient between the punch and the sheet is set to 0.2. The simulation scheme is explicit dynamic analysis with overall simulation time of 0.001 s as the constitutive material model is assumed to be rate independent. As this time scaling technique allows to benefit from the high computational efficiency, it should be kept in mind that scaling time too much in explicit simulation scheme could lead to instability due to its conditionally stable behavior.^[34]

5.2. Submodel

After finishing the macroscopic simulation, the hole expansion sheet output database file is analyzed to identify its critical region. The submodeling technique takes only this region into account and removes all the rest. The nodal displacement from the macroscopic simulation is considered as the submodel's boundary condition. The free-edge surface of the hole expansion sheet, which is perfectly smooth in the previous simulation, is replaced by the artificial surface as characterized from paragraph 4.

The raster points given from inverse Fourier transformation as shown in Figure 7a are imported to ABAQUS. This point cloud is divided into equidistance cross sections. Each cross section connects its own dots as a wire frame using a spline function. Afterward, loft feature is applied to connect wire frames to generate a solid box as shown in Figure 7b. The top surface, which represents the free edge surface, is partitioned again into smaller regions to assist the meshing operation shown in Figure 7c. The meshing is assigned on the geometry by hexahedral brick elements with reduced integration (C3D8R) with coarser mesh at the lower region.

5.3. Scalebridging

This works emphasizes that taking into account only the critical element of the macroscale provides insufficient information to perform accurate FE simulations. Therefore, wrapping the discovered behavior from the submodel to the macroscale leads to better representation of the simulation. The surface factor c_s , which has been introduced in Equation (9), plays its role at this stage. On the one hand, the damage initiation plastic strain of the mesoscale $\bar{\epsilon}_{\text{meso}}^i$ is defined by the average of equivalent plastic strain of every element in the submodel. On the other hand, the damage initiation plastic strain of the microscale $\bar{\epsilon}_{\text{micro}}^i$ is demonstrated by the equivalent plastic strain of elements within the radius of $5\mu\text{m}$ from the critical point of the submodel simulation. Comparing them together gives a hint on how much the macroscale simulation overlooks the geometrical effects in a smaller level.

6. Results

6.1. Experimental Results

A series of hole expansion sheet specimens were tested until a through-thickness crack appeared on the hole edge. A deformed sheet before the testing is shown in Figure 8a. At the point of crack initiation, the crack starts from its bottom and the middle

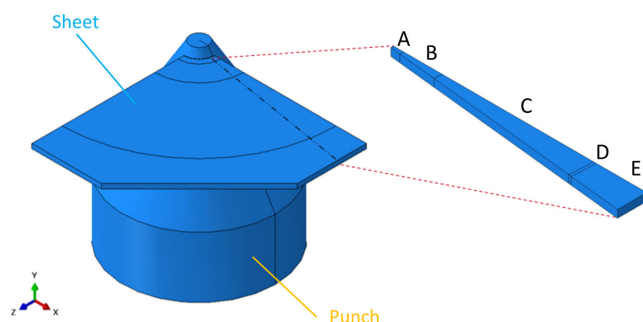


Figure 6. FE geometry of hole expansion sheet and punch.

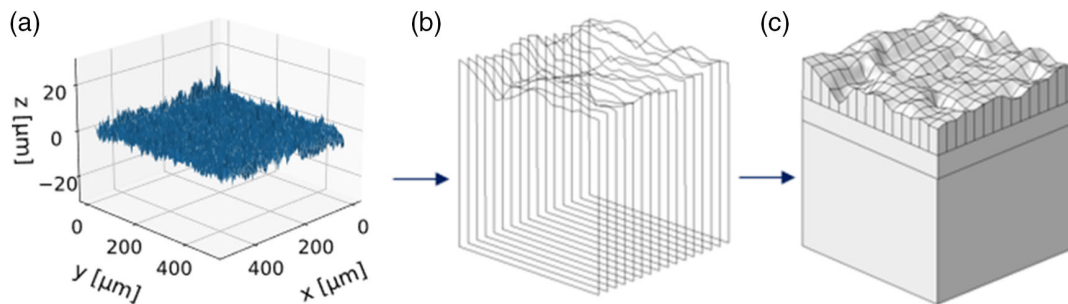


Figure 7. a) Raster point cloud from inverse Fourier transformation; b) wire cross sections constructed from the point cloud; and c) submodel with artificial surface from connected cross sections.

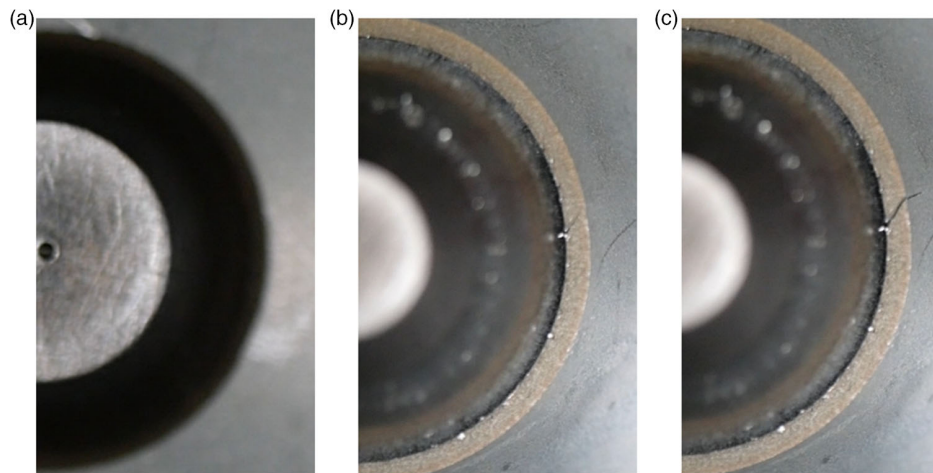


Figure 8. Top view of the hole expansion sheet a) before the experiment, b) at the crack initiation, and c) at the through-thickness crack.

of the sheet, as shown in Figure 8b. One thing to note is that the cracking behavior of this hole edge is different than cracking in the sheet with hole from the conventional punching process. The crack from that process introduces from the top of the sheet and progresses downward. It is implied that the predamage from normal manufacturing processes causes the damage initiation on the region where one loading case is applied. Once the predamage factor is reduced by using wire cutting process for edge manufacturing, it is not sufficient to provoke the damage in that region but others instead. The test stops once the crack develops through thickness of the sheet, as shown in Figure 8c. The inner diameter of the hole at this stage is used to calculate the HER. The force–displacement curve is recorded during the process to compare with the simulation results.

6.2. Macroscopic FEM Model

The HET is simulated at first to evaluate its response under an assumption that the surface condition does not play a role in the damage and fracture behavior. The force–displacement curves of the full model (360° revolution) and the reduced model (10° revolution) are compared to ensure the validity of the model reduction, as shown in Figure 9. The reduced model shows a perfect tracking to the full model until its fracture. The force from reduced model drops slightly later than the full model. In

addition, the crack from both models starts from their bottom to top according to what is observed from the experiment but with vertical development instead of diagonal development in the experiment. With its computational efficiency of 36:1, it is worth to trade-off this discrepancy. From this point on, all the simulations make use of the reduced geometrical model.

There are three different local regions whose local responses are of interest. The first region is the top region where the

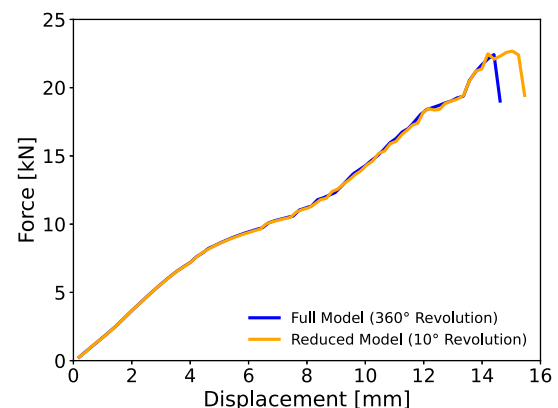


Figure 9. Force–displacement comparison between HET full model simulation and reduced model simulation.

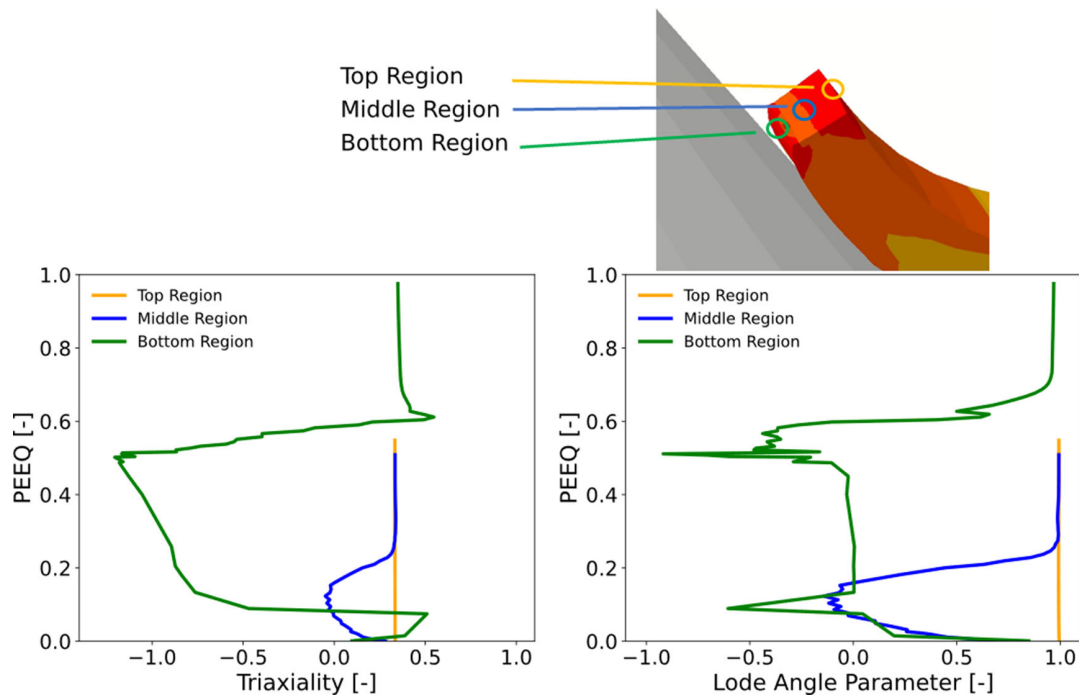


Figure 10. Strain paths at different regions in the hole expansion simulation.

conventional HET demonstrates its crack initiation. The loading case applied on this region is simply uniaxial tension. The next region is located slightly lower than the middle of the sheet. The macroscopic FE simulation indicates that this region experiences the highest damage accumulation, thus crack initiation. There are two loading cases in this region—pure shear at first and then uniaxial tension. The last region is the bottom region where the crack from the experiment initiates. In general, the loading case in this region is compression which does not induce any ductile damage. The strain paths which indicate the loading cases of these three regions are shown in **Figure 10**.

6.3. Submodel

The information from local regions provides the loading cases that the critical elements experience. Nevertheless, the macroscopic FE model only assumes the free-edge surface to be perfectly flat due to the scaling limitation of the macroscopic FE calculation. With the submodeling technique used here, the

displacement of nodes at the boundary of the critical region (or interpolation of displacement between nodes if the boundary is not located exactly on nodes) is used as input. In addition, the submodel's hole free edge is replaced by the artificial roughness from topography measurements. The multiscale strategy is illustrated from bigger scale to smaller scale in **Figure 11**.

The submodel is generated on the region where the macroscopic FE simulation indicates the highest damage accumulation, which is the middle region. **Figure 12** shows simulation results of the submodel. Herein, the top surface represents the free edge with characteristic roughness features. It is noted that there are multiple regions that show the localization on the surface. Only the spot with the highest equivalent plastic strain is taken into account for surface factor calibration.

6.4. Surface Factor Calibration

The local region which displays the highest equivalent plastic strain (PEEQ) on the surface as well as all elements within

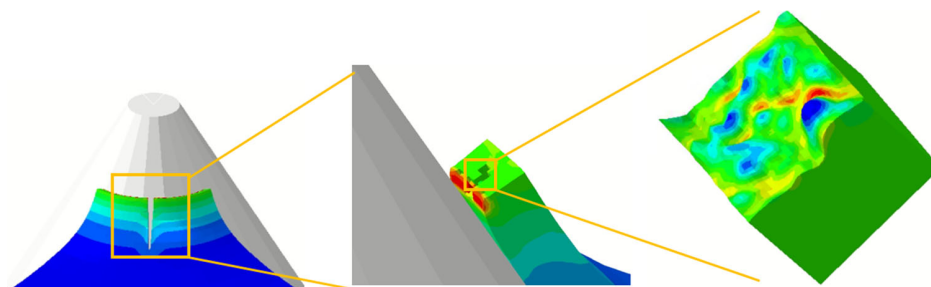


Figure 11. Multiscale strategy linking from the macroscopic simulation which informs the location and time instant of crack initiation.

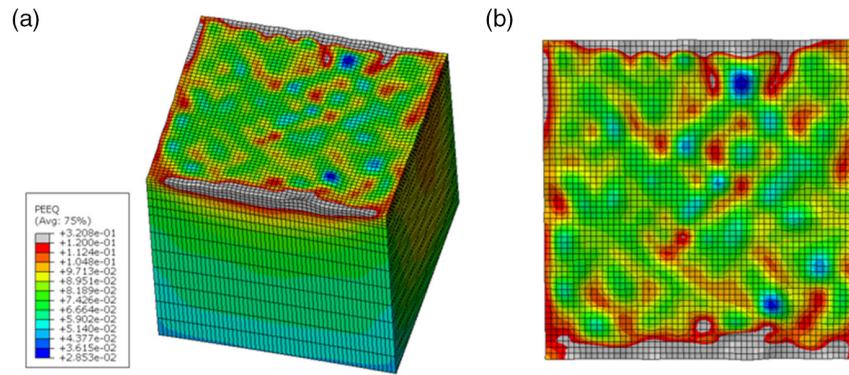


Figure 12. Submodel simulation result with artificial top surface reconstructed from measurement data in a) isometric view and b) the view normal to edge surface.

5 μm radius are included as the local region for the surface factor calibration. The volume-average strain path of this region and the volume-average strain path of the whole submodel are compared in **Figure 13**. The two crosses on each curve indicate the time step in which the damage of the local region initiates. The PEEQ at these two points are calculated as the surface factor $c_s = 0.63$.

6.5. Validation

The experimental results of the HET and its simulation results are compared. The simulations include the condition where a perfectly smooth surface condition at the hole edge is assumed; in other words, the surface factor $c_s = 1$, as well as the condition where the calibrated surface factor $c_s = 0.63$ is applied on the

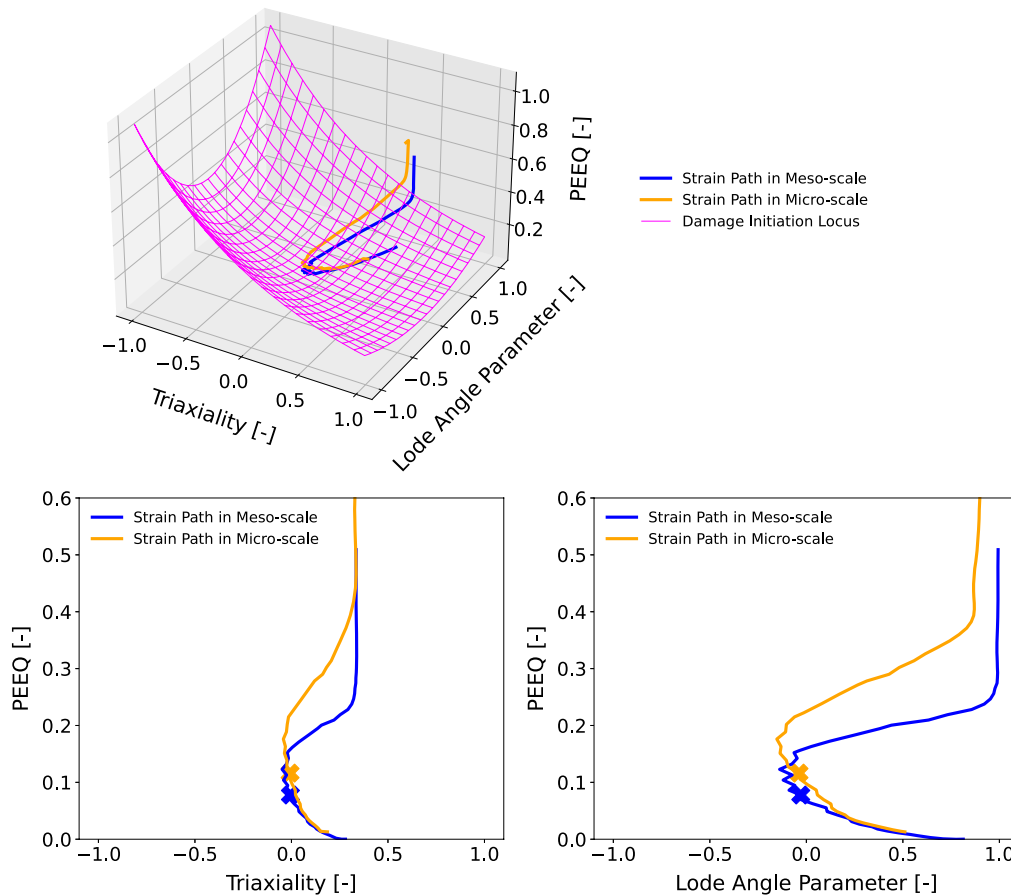


Figure 13. Comparison of strain paths of the local region (microscale) and the whole submodel (mesoscale) with indication of damage initiation time-step on the local region.

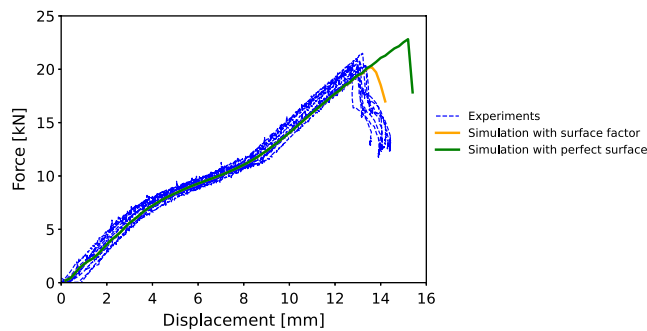


Figure 14. Force–displacement curves of HET experiments, simulation with ductile damage model at its perfect surface condition $c_s = 1.00$, and simulation with ductile damage model at surface factor $c_s = 0.63$.

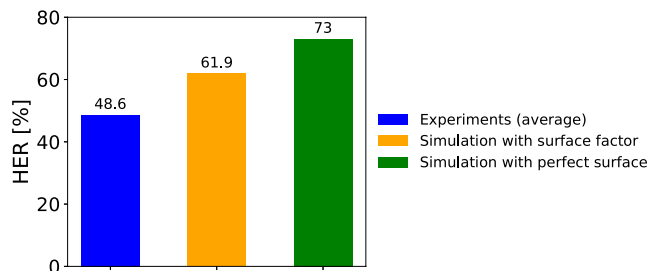


Figure 15. Comparisons of HER between the average of the experiments, simulation with ductile damage model at its perfect surface condition $c_s = 1.00$, and simulation with ductile damage model at surface factor $c_s = 0.63$.

hole edge elements. The resulting force–displacement curves as well as their HER are shown in **Figure 14** and **15**, respectively. From the force–displacement curves, the ductile damage model without surface factor consideration overestimates the fracture displacement from 13 to 15 mm. Once the model considers the surface factor, the prediction of fracture displacement becomes much closer to the experiments. In addition, considering the HER, the conventional ductile damage model overestimates the damage capacity of the steel sheet for 24.4%. With the surface factor included into the ductile damage model, it reduces the discrepancy to only 13.3%.

7. Conclusions

- 1) This study reveals the influences of surface condition in HET.
- 2) The FE simulation with the MBW ductile damage model is able to capture the material behavior of a dual-phase steel in elastic and plastic region but there are still discrepancies remaining for fracture behavior prediction reflected by force–displacement curve and HER.
- 3) The multiscale simulation technique includes the surface condition by extracting the roughness from surface measurement and reconstructing it in the 3D submodel. The novel approach can significantly reduce the discrepancy between experiment and simulation.
- 4) As the HET is a complicated process, this work introduces how to take the hole surface geometrical factor into the ductile damage model. In fact, there are still other factors that have not been introduced in the model, for

example, predamage from hole edge manufacturing process, nonlinear damage evolution from the complex loading case, and so on.

Acknowledgements

Open access funding enabled and organized by Projekt DEAL.

Conflict of Interest

The authors declare no conflict of interest.

Data Availability Statement

Research data are not shared.

Keywords

dual-phase steels, ductile damage model, finite element, roughness, surface

Received: July 19, 2021
Revised: September 20, 2021
Published online:

- [1] J. Lian, J. Wu, S. Münstermann, *Int. J. Damage Mech.* **2014**, 24, 383.
- [2] S. Münstermann, J. Lian, W. Bleck, *Int. J. Mater. Res.* **2012**, 103, 755.
- [3] J. Lian, M. Sharaf, F. Archie, S. Münstermann, *Int. J. Damage Mech.*, **2013**, 22, 188.
- [4] B. Wu, X. Li, Y. Di, V. Brinnel, J. Lian, S. Münstermann, *Fatigue Fract. Eng. Mater. Struct.* **2017**, 40, 2152.
- [5] W. Liu, J. Lian, S. Münstermann, *Eng. Failure Anal.* **2019**, 106.
- [6] F. Pütz, F. Shen, M. Könemann, S. Münstermann, *Int. J. Fracture* **2020**, 226, 1.
- [7] J. Besson, *Int. J. Damage Mech.* **2010**, 19, 3.
- [8] G. R. Johnson, W. H. Cook, *Eng. Fract. Mech.* **1985**, 21, 31.
- [9] Y. Bai, T. Wierzbicki, *Int. J. Plasticity* **2008**, 24, 1071.
- [10] G. Deng, K. Nagamoto, Y. Nakano, T. Nakanishi, *presented at the ICF12*, Ottawa, **2009**.
- [11] A. Javidi, U. Rieger, W. Eichlseder, *Int. J. Fatigue* **2008**, 30, 2050.
- [12] S. K. Ås, B. Skallerud, B. W. Tveiten, *Int. J. Fatigue* **2008**, 30, 2200.
- [13] J. Lai, H. Huang, W. Buising, *Proc. Struct. Integrity* **2016**, 2, 1213.
- [14] H. B. Xie, Z. Y. Jiang, W. Y. D. Yuen, *Tribol. Int.* **2011**, 44, 971.
- [15] P. Wechsuanmanee, J. Lian, W. Liu, S. Münstermann, *Steel Res. Int.* **2020**, 91, 2000141.
- [16] A. McMillan, R. Jones, D. Peng, G. A. Chechkin, *Meccanica* **2018**, 53, 2411.
- [17] H. A. Lauwerier, *Fractals: Endlessly Repeated Geometrical Figures*, Princeton University Press, Princeton **1991**.
- [18] P. Wechsuanmanee, J. Lian, F. Shen, S. Münstermann, *Int. J. Mater. Forming* **2020**, <https://doi.org/10.1007/s12289-020-01576-7>.
- [19] J. Lemaitre, *A Course on Damage Mechanics*, Springer, Berlin **1992**.
- [20] W. Liu, J. Lian, S. Münstermann, C. Zeng, X. Fang, *Int. J. Mech. Sci.* **2020**, 176, 105534.
- [21] S. Münstermann, J. Lian, F. Pütz, V. Brinnel, *J. Phys.: Conf. Ser.* **2017**, 896, 12074.
- [22] ISO16630, *Metallic materials—Sheet and strip—Hole expanding test* **2017**.

- [23] ISO4287, *Geometrical Product Specifications—Surface Texture; Terms, definitions and surface texture parameters* **1997**.
- [24] A. Boryczko, *Metrol. Measur. Syst.* **2010**, 17, 611.
- [25] S. Priyabrata, *Speech Processing in Embedded Systems*, Springer US, Boston, MA **2010**.
- [26] ISO16610-21, *Geometrical Product Specification (GPS)—Linear profile filters: Gaussian filters* **2011**.
- [27] ISO16610-61, *Geometrical product specification—Robust profile filters—Gaussian regression filters* **2015**.
- [28] S. W. Smith, *The Scientist & Engineer's Guide to Digital Signal Processing*, 2nd ed., California Technical Publishing, San Diego, CA **1999**, <http://people.ciirc.cvut.cz/~hlavac/TeachPresEn/11ImageProc/12FourierTxEn.pdf>.
- [29] V. Hlaváč, Fourier Transform, in 1d and in 2d (accessed: October).
- [30] W. H. Press, *Numerical Recipes: The Art of Scientific Computing*, Cambridge University Press, Cambridge, UK **2007**.
- [31] SciPy, Fourier Transforms (Scipy.fft), <https://docs.scipy.org/doc/scipy/reference/generated/scipy.fft.html> (accessed: December 2020).
- [32] Y. B. Yuan, W. Y. Piao, J. B. Xu, *J. Phys.: Conf. Ser.* **2007**, 48:1401.
- [33] Scikit-learn, R^2 Score, the Coefficient of Determination, https://scikit-learn.org/stable/modules/model_evaluation.html (accessed: December 2020).
- [34] F. Dunne, N. Petrinic, *Introduction to Computational Plasticity*, Oxford University Press, Oxford **2006**.
- [35] N. Habibi, F. Pütz, V. Brinnel, S. Münstermann, M. Feistle, W. Volk, *IOP Conf. Ser.: Mater. Sci. Eng.* **2018**, 418.